Dry tribology and nanomechanics of gaseous flame soot in comparison with carbon black and diesel soot

H Bhowmick, S K Majumdar and S K Biswas

Proceedings of the Institution of Mechanical Engineers, Part C: Journal of Mechanical Engineering Science 2012 226: 394 originally published online 22 November 2011
DOI: 10.1177/0954406211429410

Dry tribology and nanomechanics of gaseous flame soot in comparison with carbon black and diesel soot

H Bhowmick[1], **S K Majumdar**[2], and **S K Biswas**[1]*
[1]Mechanical Engineering Department, Indian Institute of Science, Bangalore, India
[2]Indian Oil Corporation Ltd. (R&D), Faridabad, India

The manuscript was received on 5 September 2011 and was accepted after revision for publication on 19 October 2011.

DOI: 10.1177/0954406211429410

Abstract: Ethylene gas is burnt and the carbon soot particles are thermophoretically collected using a home-built equipment where the fuel air injection and intervention into the 7.5-cm long flame are controlled using three small pneumatic cylinders and computer-driven controllers. The physical and mechanical properties and tribological performance of the collected soot are compared with those of carbon black and diesel soot. The crystalline structures of the nanometric particles generated in the flame, as revealed by high-resolution transmission electron studies, are shown to vary from the flame root to the exhaust. As the particle journeys upwards the flame, through a purely amorphous coagulated phase at the burner nozzle, it leads to a well-defined crystalline phase shell in the mid-flame zone and to a disordered phase consisting of randomly distributed short-range crystalline order at the exhaust. In the mid-flame region, a large shell of radial–columnar order surrounds a dense amorphous core. The hardness and wear resistance as well as friction coefficient of the soot extracted from this zone are low. The mechanical properties characteristics of this zone may be attributed to microcrystalline slip. Moving towards the exhaust, the slip is inhibited and there is an increase in hardness and friction compared to those in the mid-flame zone. This study of the comparison of flame soot to carbon black and diesel soot is further extended to suggest a rationale based on additional physico-chemical study using micro-Raman spectroscopy.

Keywords: soot, tribology, nanomechanics, wear, friction, tribofilm, Raman

1 INTRODUCTION

Soot is a carbonaceous material produced as a result of the incomplete combustion of fuels (gasoline, diesel, etc.). In diesel engine lubrication, soot has long been recognized as the major contaminant that is detrimental to engine lubrication, particularly in friction and wear. From the studies of different tribometric contacts, wear of engine components is believed to be abraded [**1**–**8**] by harder soot particles or the polishing of the steel surfaces [**1**, **8**]. Besides, the influence of a huge number of variables (size, structure, aggregation, viscosity, additive influence, etc.) present in these complex tribology contacts makes the situation even more complex to quantitatively analyse it. In this complex scenario, where many opposed effects are playing their roles in soot tribology, the influence of physical and mechanical properties of soot on the engine tribology is the least explored field. More relevant studies on this aspect can be found in the literature [**9**–**11**]. Some notable structural characterizations of flame soot were done by high-resolution transmission electron microscopy (HRTEM) [**12**–**15**]. Still, limited information is available on how such structures relate to mechanical properties and promote specific aggregations at contact, induced by tribological stresses.

In this article, the focus is on the effect of size, morphology, and crystallography of soot particles on their mechanical strength and tribological properties.

**Corresponding author: Mechanical Engineering Department, Indian Institute of Science, Bangalore 560012, India.*
email: skbis@mecheng.iisc.ernet.in

In our earlier paper, it was reported [**11**] that microstructure and graphitization of these particles vary with flame temperature along the height of the flame. In this article, investigation is made on the tribological effects of physical and microstructural properties of flame soot particles as well as those of diesel soot and carbon black. To enable the controlled variations of the physical and geometric parameters of laboratory generated soot particles, ethylene gas is burnt to thermophoretically collect soot particles at the different axial locations of the flame along the flame central axis. The particles are structurally characterized by HRTEM and Raman microspectroscopy. The hardness of a single particle is measured in a nano-indenter and related to the morphological and hardness data to friction and wear, which were recorded using an atomic force microscope (AFM) and a microtribometer.

2 EXPERIMENTAL DETAILS

2.1 Transmission electron microscopy study

Flame soot particles were directly collected on transmission electron microscope (TEM) Cu grid coated with lacy carbon layer (Pelco International, USA) and then desiccated overnight for the TEM studies. HRTEM images were obtained using a Tecnai T-20 200 kV TEM having a W-source and a point–point resolution of 1.9 Å. HRTEM images were processed using image analysis software ImageJ. The images were digitized and then converted to frequency domain by fast Fourier transform (FFT), where it was filtered through 3.3–4.5 Å bandwidth followed by an inverse FFT of the image. This processed image is then considered for fringe analysis.

2.2 Hardness measurement by nano-indentation

For indentation, the particles were deposited on cleaned silicon wafer substrates. Indentation was performed on particles in the non-imaging mode in five matrices of 30 indents each using a diamond cube corner tip of 40 nm radius, 1141 GPa Young's modulus, and 0.07 Poisson's ratio (Hysitron Triboindenter, Hysitron Inc., MN, USA). The loading was maintained in the low load range (20 and 100 μN) to avoid substrate effect, particle slipping, and particle fracture. The loading, unloading, and hold times were maintained at 5 s each. From the load–displacement curve (Appendix, Fig. 9), hardness was estimated using the Built-in software (based on the Oliver and Pharr [**16**] analysis).

2.3 Lateral force measurement by AFM

Lateral force measurements (LFMs) were performed in an AFM 'Innova' (Veeco, Santa Barbara, USA) using rectangular-shaped phosphorus (n) doped Si cantilever coated with diamond-like carbon having a spring constant of 5 N/m stiffness (Veeco, Santa Barbara, USA) and a 20-nm working tip radius. The radius of the tip was maintained and periodically checked by scanning force microscope. The cantilever normal stiffness was calibrated by methods of dimensioning [**17**] and thermal vibration [**18**]. Cantilever calibration for normal and LFMs was carried out as reported earlier [**19**]. The deflection signal was recorded here in Voltage instead of nanoampere. Before the start of each experiment, the tip was cleaned in an Ultra Violet chamber (Bioforce Nanoscience, USA) for 15 min. To enable lateral force studies on a single particle, particles collected from the flame on a silicon wafer and diesel soot and carbon black particles were suspended in *n*-hexane (99.9 per cent pure, Sigma–Aldrich). A few drops of each suspension were deposited on a silicon wafer which had been freshly coated with a thin layer of polymethyl-methaacrylate. The particles were then anchored to the substrate. The assembly was desiccated overnight.

2.4 Tribology experiments

Tribological experiments were carried out using a ball on flat microtribometer (CSM Instruments, Switzerland) in the reciprocating mode. A 2-mm diameter, acetone- and UV-cleaned, steel (DIN 100Cr6) ball was used. Polished and UV-cleaned EN31 steel was used as the substrate. During sliding, the friction coefficient was continuously estimated by measuring the X and Z displacements of the cantilever. For dry tribology tests, a few drops of the suspension of well-dispersed particle suspension in *n*-hexane (3 per cent, w/v) were sprayed on the steel substrate. The particle-coated substrate was kept in an oven at approximately 100°C for 10 min to allow the liquid to evaporate from the surface. The normal load used for all the experiments was 700 mN.

2.5 Optical profilometry

To monitor the track wear and track conditions, optical profilometry was performed with a 3D WYKO NT1100 (Wyko-MAR Precision System Inc., CA, USA) optical profiling system, and the subsequent profile analysis was done by VEECO (Vision 32) software.

2.6 Raman microspectroscopy

Raman microspectroscopy study was done for further structural studies of soot particles and to examine the tribofilm on steel substrates. Raman spectra were recorded at room temperature with a standard backscattering reflex micro-Raman spectrometer (Renishaw, System 2006; InVia), which consisted of a light microscope (Leica) coupled to a Raman spectrometer. The excitation was a diode laser of wavelength 785 nm and maximum source power 300 mW accompanied with different optical filters to adjust the required incident power. The instrument was calibrated against the Stokes Raman signal of pure Si by utilizing the first-order phonon band at 520 cm^{-1} using a silicon wafer ((1 1 1) crystal plane surface). Instrument control and spectral analysis were performed with the software packages Renishaw WiRE3.2 (Renishaw). The spectra were being studied for the first-order Raman spectra behaviours of soot.

3 RESULTS AND DISCUSSIONS

3.1 Structure

Figure 1 shows the HRTEM images of diesel soot (Fig. 1(a)), carbon black (Fig. 1(b)), and a mid-flame soot (Fig. 1(c)) particle extracted from the mid-flame region. Figure 1(d) gives a processed image of the mid-flame soot from which the interplanar spacing (d_{002}) of the particles can be calculated. Figure 1 shows that the outer shell of all the soots are graphitized to different extents, exhibiting short-range crystalline order in small but (crystallographically) bent crystallites, roughly parallel and equidistant. Such a structure of soot has been designated as 'turbostratic graphitic'. The interplanar spacing and crystallite length of different types of soot are shown in Fig. 2. These parameters are reported as a function of location of the flame from where particles were extracted. From earlier HRTEM image analysis [**11**] of the soot collected from different flame zones, it is found that the soot particles from flame root are uniformly disordered, mid-flame soot particles are more positionally configured (columnar–radial) with crystallinity and top soot particles are again disordered with randomly distributed short-range crystallinity. Interplanar spacing provides an indication of the degree of ordering or graphitization of these particles and sometimes the crystallite size within the carbonaceous material. A possible explanation for the reduction in interplanar spacing of graphitic layers near the middle flame region is densification of

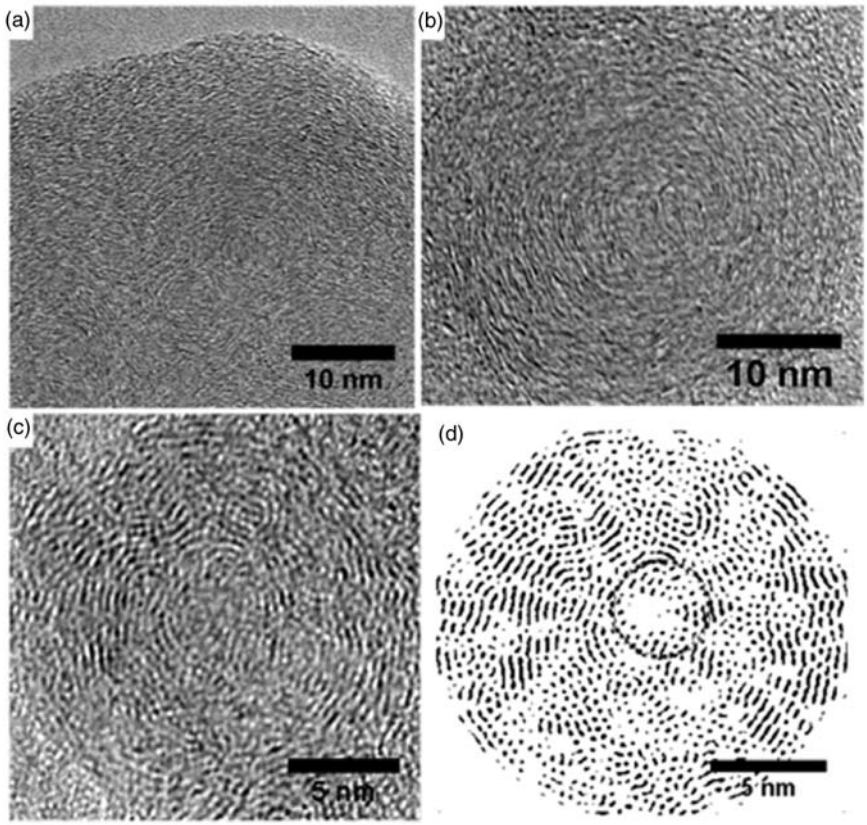

Fig. 1 Structures of (a) diesel soot, (b) carbon black, and (c) mid-flame soot; (d) processed HRTEM image of mid-flame soot particle showing inner core and outer shell

graphitic layers (since it is still in the growth stage). Thermal annealing and carbonization occur when soot after inception at the flame root passes through the peak temperature region (near $h = 2$ cm) and moves towards the lower temperature region in the downstream of the flame along the flame centre-line. As it moves further downstream and at lower temperatures, breakdown of these layers occurs due to the thermal straining leading to an interplanar spacing which is slightly larger and a crystallite length which is smaller than those found in the mid-flame zone. The soot growth also stops downstream. Generally, a reduction in d_{002} correlates with growth in the size of the ordered crystallite. However, the trend of crystallite length observed here does not give a clear indication of such a phenomenon. This may be due to the fact that the analysis was done on selected fringes and particles. Only a few graphitic layers were found in upstream, compared to the large number of such layers downstream. Carbon black shows a structure similar to that of mid-flame soot. On the other hand, diesel soot, besides the outer shell of graphitic layer, consists of a few fine particles with spherical nucleus inside a core which is surrounded by the outer graphitic shell. The crystallite length of diesel soot is of the order of that of the mid-flame soot and well below that of the carbon black.

First-order Raman spectra of different soot particles using the five band theory [**20**] are analysed here. Table 1 gives the first-order Raman spectral parameters of different dry soot particles. Table 1 (D1 full width half maximum (FWHM)) shows the middle soot to be most graphitic and least reactive of all the three flame soot particles. This observation accords well with the relative intensity data of D3 band ($I_{D3/(G+D2+D3)}$) and indicates that the abundant molecular carbon [**21**] at the flame root oxidizes and undergoes graphitic transformation while approaching the mid-flame region. It is observed earlier [**11**] that this well-ordered global structure in the mid-flame region breaks up into very short-range ordered crystallites which assemble randomly as the particle reaches the tip of the flame. The loss of order at the flame tip, which is inferred from the D1 FWHM data [**22**], is believed to be a reflection of this collapse, which is very likely caused by thermal strains as the particle moves from a high-temperature (1690 K) mid-flame region to a lower temperature (1555 K) flame tip (Fig. 3). Figure 3 shows an estimated variation of temperature along the flame axis. It is quite likely that the soot temperature may also play a role in

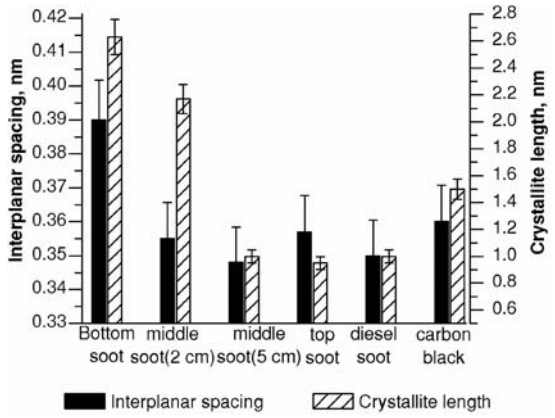

Fig. 2 Average interplanar spacing and crystallite length for different soot particles

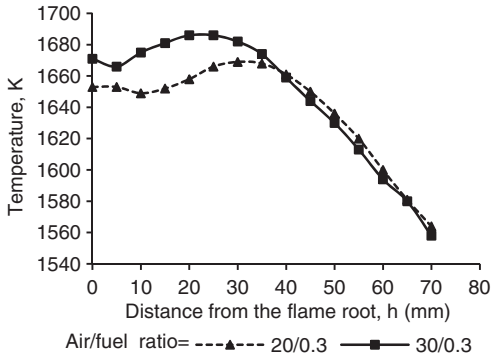

Fig. 3 Measured temperature profile of a flame along the central axis for two different air/fuel ratios. All the subsequent analyses are for the particles collected at air/fuel ratio = 30/0.3

Table 1 First-order Raman spectral parameters of un-slid dry particles

Soot type	Intensity ratio			FWHM D1
	$I_{D1/G}$	$I_{D3/G}$	$I_{D3/(G+D2+D3)}$	
Bottom	3.00	0.910	0.344	181
Middle	2.10	0.470	0.222	140
Top	2.80	0.690	0.292	170
Diesel	2.29	0.316	0.387	142
Carbon black	1.90	0.550	0.286	160

determining mechanical properties, especially in the upper regions of the flame (between 4 and 7 cm from the flame root).

The flame soot also has lower organic content than the diesel soot and this suggests lower reactivity of the flame soot than the diesel soot. Carbon black shows similar characteristic in this respect as the flame soot. The molecular carbon content of the diesel soot (from $I_{D3/(G+D2+D3)}$) is high, which is in the form of oxides and carbonyls, thus making the diesel soot surface more reactive than the other soots.

Figure 4 shows a typical particle size distribution of the single particle, averaged from TEM images, along the flame axis and for carbon black and diesel soot. It shows that for the flame soot, the primary particles increase in diameter with h (distance from the flame root) till about $h = 4$ cm; at $h > 4$ cm, there is a reduction in primary particle size due to the competition of simultaneous surface growth and oxidation. Hurt *et al.* [**23**] report a reduction in the size of primary particles with increasing distance from the flame root, due to progressive sintering and collapse. On the other hand, the diameters of the cores consistently reduce with increasing h till a distinct central core disappears at $h = 7$ cm. Reduction of the core diameter with increasing distance from the flame root (decreasing temperature) has been rationalized by Hurt *et al.* [**23**], who argue that the total free energies of the system, consisting of the elastic strain and the orientational energies, are minimized to give the core radius. The core radius is shown to be inversely proportional to $(T_c - T)$, where T_c is the flame root temperature and T the temperature at any location along the flame except at the location above the flame root, where the soot is superheated than the flame root temperature.

3.2 Hardness

Figure 5 shows the hardness of single soot particles collected at different values of h of flame as well as for carbon black and diesel soot. It is believed that the sequence, shell thickness, shell disorder, and core volume in the particles, which is observed in Fig. 4 with increasing h, has a major impact on the mechanical property variation of the soot along its axis. It appears that the uniformly disordered material present close to the flame root is softer than the disordered material which harbours randomly distributed short-range crystallinity. The effect of a more positionally configured (columnar–radial) crystallinity appears to make the material less stiff than the mainly disordered soot present at $h = 0.5$ cm.

Field and Swain [**24**] suggest that the deformation of carbon material in indentation is mechanistically controlled by inter-crystalline slip along the basal plane of the graphitic nanocrystals, besides the elastic penetration mechanism. According to this suggestion, one would expect particles composed of stacked layers of graphite crystallites to easily deform and yield low hardness compared to that of particles where such mechanism is not available. For example, for particles which are more graphitic in nature, more is the chance of interplanar slip causing low hardness than more amorphous carbon materials. The molecular carbon content of the diesel soot is higher than the flame soot. The diesel soot consists of oxides and carbonyls. This makes the diesel soot surface more reactive and harder than those of the other soot

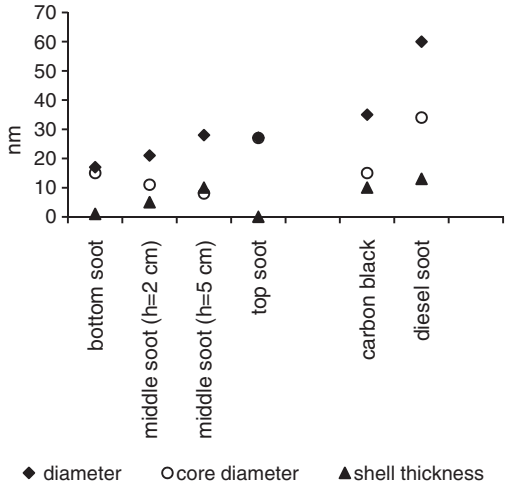

Fig. 4 Average particle sizes, core diameters, and shell thicknesses of different flame soot particles, carbon black and diesel soot

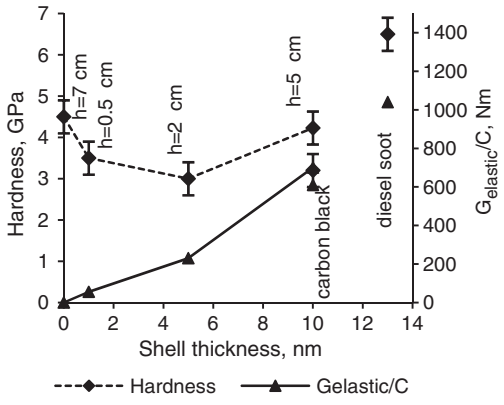

Fig. 5 Hardness and elastic energy as the function of ordered graphitic shell thickness of different soot particles, where C is a geometric constant and the estimate of elastic energy is as per the formulation of Hurt *et al.* [**23**]

particles. In addition, there is also a possibility that nano-size particle consisting of hard amorphous products may be incorporated within the turbostratic structure of soot particles resulting in high hardness of diesel soot.

Another possible way to rationalize the data is in terms of stored elastic energy. The formulation of Hurt *et al.* [**23**] gives the elastic energy, $G_{elastic} = C \times E \times s$, where C is a geometric constant, E the Young's modulus, and s the shell thickness (the inner surface of the shell marks the order–disorder phase boundary). By this formulation, when there is an order-to-disorder phase change, in the present case, such a change happens between $h = 2$ and 5 cm (shell thickness between 5 and 10 nm), and the elastic energy increases with the thickness of the outer shell of the soot particles. Figure 5 shows an increase in $G_{elastic}/C$ with shell thickness in this range of shell thickness. Hardness indicates that resistance to dislocation glide and obstacle to such a glide increase the elastic energy of the system and hardness. There is thus a possible correlation between stored elastic energy and hardness, where there is a clear order to disorder transition. The model proposed by Hurt *et al.* [**23**] may thus provide a rationale for the hardness variation when there is a clear coexistence of crystalline and disorder phases in a soot particle. The model may not be valid in the 0–4 nm shell thickness range, where the amorphous core predominates. Accordingly, diesel soot, going by this rationale, should have higher hardness than the flame soot. Without further corroborative experimental work, it is not possible at this stage to conclusively indicate the validity of any or a combination of the above reasoning.

From the hardness measurements, it is evident that the diesel soot is much harder than the flame soot and the commercial carbon black, and the carbon black's hardness lies within the range of those of the flame soot. The reason for the high hardness of diesel soot is, besides the above rationale, the complex combustion (liquid fuel) chemistry involved in a diesel engine environment and the subsequent heat treatment that happens in the hot diesel engine combustion chamber environment.

3.3 Tribology

Figure 6 shows the trend and scatter in thickness of material removed in the LFM experiments as a function of normal load. It shows that the amount of soot removed under traction in the LFM is the lowest when the particles are most disordered as they are near the flame root ($h = 0.5$ cm) and at the top of the flame ($h = 7$ cm). The shear strength of the flame

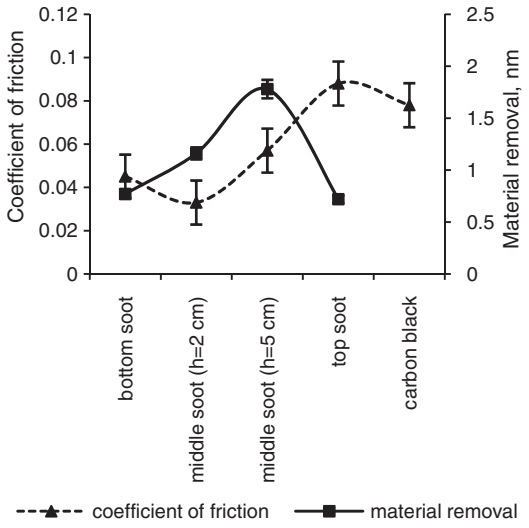

Fig. 6 Coefficients of friction and material removal at normal load of 200 nN, for different types of soot measured by LFM

particle when calculated from friction force by scan area is found to be in the range 0.5–3 MPa, varying from the more ordered to the more disordered state of particles. Thus, when the particles are scratched by an AFM tip, the ordered layered materials are more prone to get displaced than the disordered layers owing to their low shear strength. At this stage, it can be surmised that the disordered particles offer more resistance to shear than that offered by the more ordered particles. This disordered structure, on the one hand, protects the soot, and on the other hand, may be responsible for abrasion of tribological components when soot is inducted into at such contacts, suspended in oil.

Here, the relationship of friction with the location in the flame (designate this as 'h', the distance of a point on the central flame axis from the flame root) from where the soot is extracted and the corresponding flame temperature is also being investigated.

Figure 7 shows the groove depth and pile-up/groove area values of the tracks formed by microtribometry tribology experiments for different tribocontacts. For the present configuration, it is very likely that the contact is fully plastic under sliding and observed pile-up is caused by plastic flow. After the wear test, if all the material deformed and displaced by indentation is accounted for in the pile-up, the pile-up area-to-groove area ratio $\rho \to 1$, and in reality, the ratio $\rho < 1$. The large groove depth and low ρ observed here are believed to be accounted for by the wear of the initial groove created by indentation. When the flame soot is used as a dry lubricant, the groove depth remains at the low level but ρ is higher

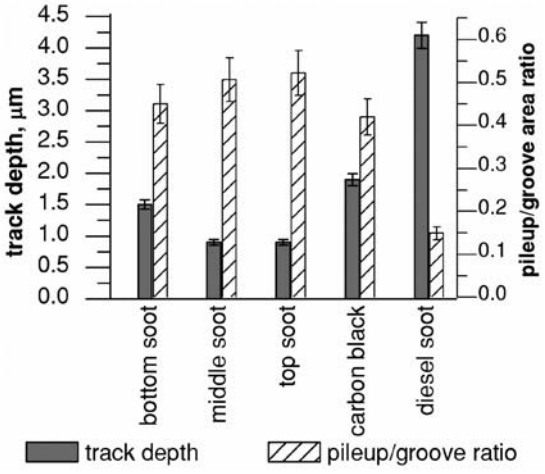

Fig. 7 Pile-up area/groove area, ρ and groove depth values measured for wear tracks (speed = 0.5 cm/s)

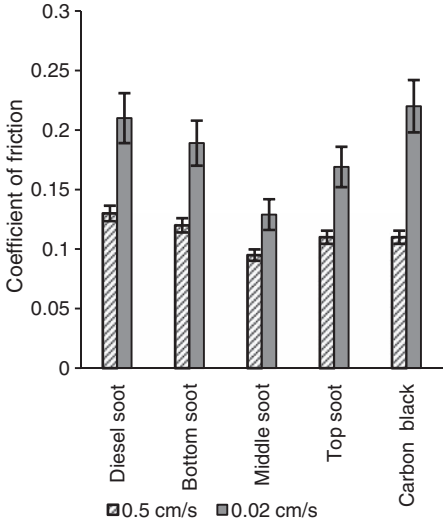

Fig. 8 Coefficients of friction from dry tribology test involving different soot samples for the linear speeds of 0.5 and 0.02 cm/s

than the diesel soot. This suggests that in the former case, there is very little wear of the substrate. The hardness of diesel soot is comparable to the hardness of the hardest parts used in the engine component, which may be one of the influential factors towards the engine abrasion due to the presence of soot. Moreover, the high molecular carbon content (Table 1) of the surface of the diesel soot in the form of oxides is known [**25**] to lead to the abrasion of a steel counterface. This soot can potentially promote wear due to its high hardness. At this stage, it can be hypothesized that in the case of flame soot, the tribofilm formed in the track is protected or remains intact once formed for the rest of the friction run and material pile-up takes place instead of any further material wear, rather due to the material displacement by plastic deformation of soot in contact or contacting steel substrate, which is evident by high pile-up/groove depth ratio. On the other hand, in case of diesel soot, due to its high hardness and abrasiveness, continuation of material wear by ploughing action predominates over the plastic deformation of substrate and continuous formation and removal of tribofilm occur followed by intermittent soot/metallic wear of the substrate, which leads to the very low value of ρ. It is logical to suggest at this stage that this difference between the conditions of the track is caused by the fact that soot particles are perpetually present at the ball/flat interface, influencing the contact by their mechanical, structural, and surface properties.

Wahl and Singer [**26**] suggested a dynamic process which leads to the formation of a tribofilm. The process consists of drawing in particles from the reservoirs which exist at the two extremities of the reciprocating stroke (normal to the sliding direction) and shearing them and dragging them in by sliding contact. The film material and thickness are conserved as the filling in of the abrasion grooves and the abrasion itself simultaneously occurs in one cycle. When no soot particles are fed into the contact, metal-to-metal contact occurs, causing wear.

The friction data presented in Fig. 8 generally show that the coefficient of friction is significantly brought down from that when the contact is a metal-to-metal one, by the development of the soot tribofilm on the substrate. First, the coefficient of friction is significantly reduced from that when there is dry metal-to-metal contact by the induction of dry soot into the contact. Second, for the flame soot, the coefficient of friction of soot is specific to the location in the flame from where the soot is extracted. In general, it is found that friction is less for middle soot, highest for bottom soot, while that of top soot friction lies between those top and middle soot particles. Diesel soot and carbon black give higher friction than the flame middle soot. Factors which may influence such a distinction may be (1) particle size as it enters the contact zone causing interference and/or(2) the physical quality and structure of the as-extracted particles, and (3) the change in the physical quality of the soot, induced by tribology.

3.4 Micro-Raman spectroscopy of wear tracks

No one-to-one correlation of agglomerate size to tribological parameters was found in this study.

Table 2 First-order Raman spectral parameters of different soot particles after dry tribology test

Soot type	Intensity ratio			FWHM D1
	$I_{D1/G}$	$I_{D3/G}$	$I_{D3/(G+D2+D3)}$	
Bottom	2.09	0.45	0.238	172
Middle	1.75	0.25	0.183	135
Top	3.44	0.48	0.291	185
Diesel	3	0.67	0.370	155
Carbon black	2.2	0.69	0.301	146

The as-extracted particles were analysed using Raman microspectroscopy and HRTEM, while the former is used to analyse the tribofilm *ex situ*. The latter gives the physical structures and their changes under dry tribology and their influence on the observed trend in the friction.

In reviewing the friction data of soot extracted from different locations of the flame as they are subjected to dry tribology, two definite trends are observed. First, the bottom and top soot friction values are always higher than the middle soot friction. Second, the diesel soot and carbon black friction values are higher than the middle soot friction.

The spectral data presented in Tables 1 and 2 are reviewed in the context of coefficient of friction data presented in Fig. 8. It can be hypothesized at this stage that graphitic structure promotes low friction in tribology as it allows basal slip at contact. In contrast, molecular carbon is likely to undergo bulk plastic deformation at contact and promote reactivity; both of such effects would tend to enhance friction. Comparing spectral data from Tables 1 and 2, it is obvious that dry tribology graphitizes the bottom soot and decreases the molecular carbon content but does not bring the graphitization and molecular carbon content to the same level as achieved when the middle soot is subjected to dry tribology (Table 2). Relative magnitudes of dry tribology spectral data between the middle, bottom, and top soot support the observed friction trends (Fig. 8). However, the molecular carbon content of the soot after dry tribology is higher than that of the corresponding un-slid particles. On the other hand, these properties are not very different from those of the carbon black particles. Diesel soot becomes more amorphous and structurally disordered after dry tribology test.

The above discussion suggests that the physical and chemical changes as recorded by Raman spectroscopy certainly contribute to the relative tribological merits of different types of soot. The soot particles generally consist of reactive molecular and graphitized carbon molecules. Other functional groups are present in the diesel soot as they emanate from the complex diesel engine environment. The presence of the molecular carbon tends to enhance friction, while the graphitized carbon tends to reduce friction. The relative extent of the two constituents determined by thermal changes along the flame axis as well as by tribology determines the aggregate frictional property of the soot material.

4 SUMMARY

Thermophoretically sampled soot at different locations of a flame generated by burning ethylene gas and industrial diesel soot and carbon black are found to have widely different morphologies, crystallographic orders, and reactivity. Graphitization and chemical reactivity *via* molecular carbon content of soot oppose each other in determining the friction of soot in tribology. The hardness, friction, and resistance to material removal of the soot collected near the flame tip and diesel soot are high. These properties of the strongly ordered soot extracted from the mid-flame region are comparatively low. The strongly graphitized as-extracted mid-flame soot is morphologically stable in tribology and promotes low friction. Due to the high hardness and more abrasive nature of diesel soot, it adversely influences the metal wear.

ACKNOWLEDGEMENTS

This study is supported by Indian Oil Corporation Limited (R&D), Faridabad, which made this study possible. The authors sincerely thank Mr. Chidananda Shetty for assisting in different experimental works, Mrs. Rashmi and Mrs. Bindu CN for assisting in nano-indentation and tribology experiments, Ducom Pvt Ltd for fabricating the soot generation rig assembly and Continental Carbon, India for providing carbon black samples.

FUNDING

This work was supported by Indian Oil Corporation Ltd (R&D), Faridabad, India [grant number 99149].

REFERENCES

1 **Berbezier, I., Martin, J. M.,** and **Kapsa, P.** The role of carbon in lubricated mild wear. *Tribol. Int.*, 1986, **19**, 115–122.
2 **Chinas-Castillo, F.** and **Spikes, H. A.** The behavior of diluted sooted oils in lubricated contacts. *Tribol. Lett.*, 2004, **16**, 317–322.
3 **Green, D. A.** and **Lewis, R.** The effects of soot-contaminated engine oil on wear and friction: a review. *Proc. IMechE, Part D: J. Automobile Engineering*, 2008, **222**, 1669–1689.
4 **Rounds, F. G.** Carbon: cause of diesel engine wear. SAE [prepr.] paper 770829, 1977.
5 **Green, D. A., Lewis, R.,** and **Dwyer-Joyce, R. S.** Wear effects and mechanisms of soot-contaminated automotive lubricants. *Proc. IMechE, Part J: J. Engineering Tribology*, 2006, **220**, 159–169.
6 **Gautam, M., Durbha, M., Chitoor, K., Jaraiedi, M., Mariwalla, N.,** and **Ripple, D.** Contribution of soot contaminated oils to wear. SAE [technical] paper 981406, 1998, Spec Pub, vol. 1372, pp. 55–67.
7 **Gautam, M., Chitoor, K., Durbha, M.,** and **Summers, J. C.** Effect of diesel soot contaminated oil on engine wear investigation of novel oil formulations. *Tribol. Int.*, 1999, **32**, 687–699.
8 **Ryason, P. R., Chan, I. Y.,** and **Gilmore, J. T.** Polishing wear by soot. *Wear*, 1990, **137**, 15–24.
9 **Liu, C., Nemoto, S.,** and **Ogano, S.** Effect of soot properties in diesel engine oils on frictional characteristics. *Tribol. Trans.*, 2003, **46**, 12–18.
10 **Jao, T. C., Li, S., Yatsunami, K., Chen, S. J., Csontos, A. A.,** and **Howe, J. M.** Soot characterization and diesel engine wear. *Lubr. Sci.*, 2004, **16**, 111–126.
11 **Bhowmick, H.** and **Biswas, S. K.** Relationship between physical structure and tribology of single soot particles generated by burning ethylene. *Tribol. Lett.*, 2011, **44**, 139–149.
12 **Shaddix, C. R., Palotas, A. B., Megaridis, C. M., Choi, M. Y.,** and **Yang, N. Y. C.** Soot graphitic order in laminar diffusion flames and a large-scale JP-8 pool fire. *Int. J. Heat Mass Transfer*, 2005, **48**, 3604–3614.
13 **Chen, Y., Shah, N., Braun, A., Huggins, F. E.,** and **Huffman, G. P.** Electron microscopy investigation of carbonaceous particulate matter generated by combustion of fossil fuels. *Energy Fuels*, 2005, **19**, 1644–1651.
14 **Palotas, A. B., Rainey, L. C., Feldermann, C. J., Sarofim, A. F.,** and **Vander Sande, J. B.** Soot morphology: an application of image analysis in high-resolution transmission electron microscopy. *Microsc. Res. Tech.*, 1996, **33**, 266–278.
15 **Ishiguro, T., Takatori, Y.,** and **Akihama, K.** Microstructure of diesel soot particles probed by electron microscopy: first observation of inner core and outer shell. *Combust. Flame*, 1997, **108**, 231–234.
16 **Oliver, W. C.** and **Pharr, G. M.** An improved technique for determining hardness and elastic modulus using load and displacement sensing indentation experiments. *J. Mater. Res.*, 1992, **7**, 1564–1583.
17 **Cleveland, J. P., Manne, S., Bocek, D.,** and **Hansma, P. K.** A nondestructive method for determining the spring constant of cantilevers for scanning force microscopy. *Rev. Sci. Instrum.*, 1993, **64**, 403–405.
18 **Hutter, J. L.** and **Bechhoefer, J.** Calibration of atomic-force microscope tips. *Rev. Sci. Instrum.*, 1993, **64**, 1868–1873.
19 **Devaprakasam, D., Khatri, O. P., Shankar, N.,** and **Biswas, S. K.** Boundary lubrication additives for aluminium: a journey from nano to macrotribology. *Tribol. Int.*, 2005, **38**, 1022–1034.
20 **Sadezky, A., Muckenhuber, H., Grothe, H., Niessner, R.,** and **Poschl, U.** Raman microspectroscopy of soot and related carbonaceous materials: spectral analysis and structural information. *Carbon*, 2005, **43**, 1731–1742.
21 **Knauer, M., Schuster, M. E., Su, D., Schlogl, R., Niessner, R.,** and **Ivleva, N. P.** Soot structure and reactivity analysis by Raman microspectroscopy, temperature-programmed oxidation, and high-resolution transmission electron microscopy. *J. Phys. Chem. A*, 2009, **113**, 13871–13880.
22 **Dippel, B., Jander, H.,** and **Heintzenberg, J.** NIR FT Raman spectroscopic study of flame soot. *Phys. Chem. Chem. Phys.*, 1999, **1**, 4707–4712.
23 **Hurt, R. H., Crawford, G. P.,** and **Shim, H. S.** Equilibrium nanostructure of primary soot particles. *Proc. Combust. Inst.*, 2000, **28**, 2539–2546. (Elsevier).
24 **Field, J. S.** and **Swain, M. V.** The indentation characterization of the mechanical properties of various carbon materials: glassy carbon, coke and pyrolytic graphite. *Carbon*, 1996, **34**, 1357–1366.
25 **Patel, M.** and **Aswath, P.** Diesel soot chemical characterization using XANES. *Tribol. Lubr. Technol.*, 2010, **66**, 17–18.
26 **Wahl, K. J.** and **Singer, I. L.** Quantification of a lubricant transfer process that enhances the sliding life of a MoS2 coating. *Tribol. Lett.*, 1995, **1**, 59–66.

APPENDIX

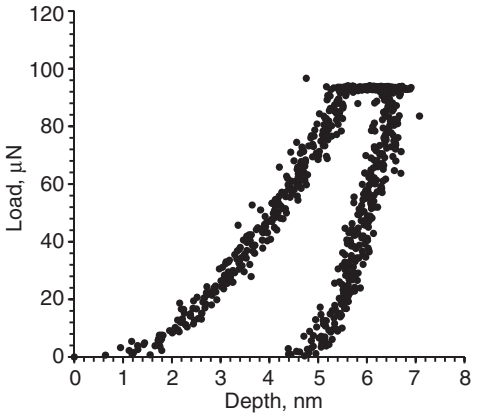

Fig. 9 Typical load–depth curve of flame soot